THE JOURNAL OF BIOLOGICAL CHEMISTRY VOL. 289, NO. 49, pp. 34241–34249, December 5, 2014

Chemical Structure and Morphology of Dorsal Root Ganglion Neurons from Naive and Inflamed Mice*

Received for publication, April 2, 2014, and in revised form, September 24, 2014 Published, JBC Papers in Press, September 30, 2014, DOI 10.1074/jbc.M114.570101

Marie E. Barabas[‡1], **Eric C. Mattson**[§1], **Ebrahim Aboualizadeh**[§], **Carol J. Hirschmugl**[§], **and Cheryl L. Stucky**[‡2]

From the [‡]*Department of Cell Biology, Neurobiology and Anatomy, Medical College of Wisconsin, Milwaukee, Wisconsin 53226-0509 and the* [§]*Department of Physics, University of Wisconsin-Milwaukee, Milwaukee, Wisconsin 53211*

Background: Roles of lipids and carbohydrates in sensory transduction are understudied.
Results: Localization of lipids and carbohydrates in neuronal subsets is identified and associated with enrichment of endoplasmic reticulum; lipids increased in nociceptors during inflammation but not in TRPA1-deficient neurons.
Conclusion: Chemical morphology varies in sensory subpopulations; TRPA1-mediated lipid increases may underlie mechanical sensitization with inflammation.
Significance: Lipids and carbohydrates may mediate inflammatory pain.

Fourier transform infrared spectromicroscopy provides label-free imaging to detect the spatial distribution of the characteristic functional groups in proteins, lipids, phosphates, and carbohydrates simultaneously in individual DRG neurons. We have identified ring-shaped distributions of lipid and/or carbohydrate enrichment in subpopulations of neurons which has never before been reported. These distributions are ring-shaped within the cytoplasm and are likely representative of the endoplasmic reticulum. The prevalence of chemical ring subtypes differs between large- and small-diameter neurons. Peripheral inflammation increased the relative lipid content specifically in small-diameter neurons, many of which are nociceptive. Because many small-diameter neurons express an ion channel involved in inflammatory pain, transient receptor potential ankyrin 1 (TRPA1), we asked whether this increase in lipid content occurs in TRPA1-deficient (knock-out) neurons. No statistically significant change in lipid content occurred in TRPA1-deficient neurons, indicating that the inflammation-mediated increase in lipid content is largely dependent on TRPA1. Because TRPA1 is known to mediate mechanical and cold sensitization that accompanies peripheral inflammation, our findings may have important implications for a potential role of lipids in inflammatory pain.

Investigation of cellular pain mechanisms is challenging because sensory neurons are exceptionally heterogeneous in terms of their transduction properties and cellular function (1–8). Dorsal root ganglia (DRG)[3] neurons send axonal projections into a variety of peripheral tissues, including skin, muscle, joints, and visceral organs. The sensory endings of subpopulations of these neurons are tuned to sense a variety of different environmental stimuli, such as light touch, painful force, and temperature changes (1, 5). Some endings sense internal stimuli such as inflammatory chemicals or changes in body temperature (9–11). Many small-diameter somata (<27 μm) correspond *in vivo* to unmyelinated C fibers that are nociceptive, or pain-sensing. Large-diameter somata (≥ 27 μm) generally have lightly to heavily myelinated Aβ or Aδ axons *in vivo*. Some of these A fibers sense innocuous tactile stimuli, whereas others are nociceptive (5, 12–14). A portion of each of these subpopulations of neurons becomes sensitized during tissue damage and inflammation and thus contributes to driving pain (1, 15). The incomplete understanding of DRG neuron subpopulations on a molecular level has limited the revelation of transduction and sensitization mechanisms, which may depend on chemical and structural properties of the plasma membrane, particularly those that involve mechanotransduction and mechanical hyperalgesia.

Specialized subpopulations of DRG neurons have primarily been characterized in terms of gene and protein expression and cellular function (1–5, 7–8). However, protein receptors lie within a complex, fluid membrane that also includes lipids and carbohydrates. In fact, lipids and carbohydrates have been shown to modulate properties of mechanotransduction in cells. For example, disruption of lipid rafts decreases mechanical sensitivity of osteoblasts and epithelial cells (16–18), and enzymatic degradation of membrane carbohydrates decreases responses to shear stress in endothelial cells (19). Lipid rafts and carbohydrates have been shown to influence excitability of DRG neurons (20–26), and these biochemicals may also modulate mechanotransduction properties of sensory neurons. Recently, altered lipid metabolism pathways have been implicated in nerve injury-induced and inflammatory pain (27–29). Therefore, it is important to consider the influence of lipids and carbohydrates in sensory neuron function in naive animals and during inflammation.

Traditional techniques to study lipids and carbohydrates require pooling samples, which does not allow for assessment of

* This work was supported, in whole or in part, by National Institutes of Health R01 Grants NS040538 and NS070711 (to C. L. S.). This work was also supported by National Science Foundation (NSF) Grant CHE-1112433 (to C. J. H.).
[1] Both authors contributed equally to this work.
[2] To whom correspondence should be addressed: Dept. of Cell Biology, Neurobiology and Anatomy, Medical College of Wisconsin, 8701 Watertown Plank Rd., Milwaukee, WI 53226-0509. Tel.: 414-955-8478; Fax: 414-955-6517; E-mail: cstucky@mcw.edu.
[3] The abbreviations used are: DRG, dorsal root ganglia; ER, endoplasmic reticulum; TRPA1, transient receptor potential ankyrin 1; CFA, complete Freund's adjuvant.

the variability between heterogeneous DRG neuron subpopulations. In contrast, the non-invasive nature of IR chemical imaging enables label-free imaging to detect the distribution and the characteristic infrared absorption peaks from proteins, lipids, phosphates, and carbohydrates simultaneously in individual DRG neurons (30). Here, we hypothesized that heterogeneous populations of sensory neurons likely differ in chemical features. Therefore, we conducted FTIR spectromicroscopy to identify DRG subpopulations based on chemistry. This is the first study to use FTIR spectromicroscopy to assess the biochemical composition of somatosensory neurons. We employed synchrotron radiation at the Infrared Environmental Imaging (IRENI) mid-infrared beamline at the Synchrotron Radiation Center (SRC; University of Wisconsin-Madison). The use of this beamline enables rapid, diffraction-limited spatial resolution imaging of individual neurons (30, 31). Importantly, this experimental approach can probe length scales that are on par with subcellular structures.

Using FTIR spectromicroscopy, we were able to visualize the distribution of chemical features and identify changes in chemistry on a single-cell basis. We identified and characterized particularly unusual architectures of chemical structures that were created by an annular "ring" distribution of carbohydrate and/or lipid enrichment in the cytoplasm in sensory neuron subpopulations, a feature that has never before been reported in native cells of any type. We also demonstrated that peripheral inflammation induces significant increases in the relative lipid content of putative nociceptors on the single-cell level, and that this change is dependent on an ion channel known to be involved in inflammatory pain, transient receptor potential ankyrin 1 (TRPA1).

EXPERIMENTAL PROCEDURES

Animals—Experiments were conducted either on male 3–6-month-old mice that were of the C57BL/6J strain (wild type; The Jackson Laboratory) or on mice with genetically ablated transient receptor potential ankyrin 1 (TRPA1 KO), which is on a C57BL/6J background (32). All experimental procedures were approved by the Institutional Animal Care and Use Committee of the Medical College of Wisconsin.

CFA Inflammation—Straight complete Freund's adjuvant (CFA, 30 μl, Sigma) was injected subcutaneously into the plantar hind paw of mice, causing marked inflammation of the entire paw and hind limb (33). Two days after injection, ipsilateral lumbar 3–6 DRGs were cultured and dissociated as described below. Lumbar DRGs 1–6 from naive mice were used as a comparison.

DRG Culture—DRGs were cultured as described previously (34, 35). The isolated neurons were plated onto laminin-coated BaF_2 windows (Pike Technologies, Madison, WI) and incubated for 2 h at 37 °C and 5% CO_2 to allow adherence. No exogenous growth factors were added. Windows were then flooded with DMEM/Hams-F12 medium supplemented with 10% heat-inactivated horse serum, 2 mM L-glutamine, 0.8% D-glucose, 100 units of penicillin, and 100 μg/ml streptomycin. Chemical imaging experiments were conducted 18–24 h after the neurons were plated because this is the time range when many patch clamp and calcium imaging recordings have been performed (35–39). Cultures were transported in humidified Petri dishes. At least three independent primary culture preparations were conducted per group consisting of DRGs from $n = 6$ wild-type naive, 7 wild-type CFA, 5 TRPA1 KO naive, and 8 TRPA1 CFA mice.

Cell Culture of Neuro2a Cells—Neuro2a cells (ATCC CCL-131) were plated onto laminin-coated BaF_2 windows and provided growth medium containing minimum essential medium (Life Technologies), 10% FBS (Life Technologies), sodium bicarbonate, non-essential amino acids, sodium pyruvate, and penicillin/streptomycin. The cells were imaged 24 h after plating.

FTIR Data Collection and Analysis—Infrared spectromicroscopy was performed at the SRC (Stoughton, WI) using the IRENI beamline (30). Briefly, the beamline extracts a large swath of radiation (320 ×25 milliradians) to homogeneously illuminate a commercial focal plane array detector. The beamline is coupled to a Bruker Vertex 70 IR microscope and a Bruker Hyperion 3000 IR microscope equipped with a focal plane array detector. The measurements were performed using a 74× Cassegrain objective with a numerical aperture of 0.65. With this experimental geometry, the effective geometric pixel size at the sample plane is 0.54×0.54 μm^2. The data were collected with 128 co-added scans at 6-cm^{-1} spectral resolution. A clean region of the laminin-coated BaF_2 substrate was used as the reference measurement. Neurons were randomly selected for imaging.

Analysis of the IR Images was performed using the software package IRidys. Chemical images were generated by calculating the area under a given characteristic peak for every pixel of the field of view, and the results are displayed as false-colored images. Assessment of chemical rings was conducted by experimenters that were blinded to treatment, genotype, and cell size. Average spectra for a given cell were calculated by defining a region of interest such that only the pixels comprising the area occupied by the cell were included in the averaging.

Tomography Data Collection and Analysis—Tomographic measurements were performed as described previously (40) with the sample mounted on a laminin-coated 50-μm polyimide microloop holder, using a 36× (NA = 0.5) magnification objective. The data were recorded over a 362° angular range at increments of 2.7°. Tomographic reconstructions were performed using custom-written analysis procedures in the open access software platform in Fiji, as described previously (41–45).

We performed tomographic reconstructions of the cell using the carbohydrate spectral region as this spectral region had features that were very distinct from the polyimide microloop holder (unlike the C–H stretching region, which was unduly influenced by dried medium on the sample holder). Additionally, ring features in sensory neurons were often observed in chemical images of the carbohydrate spectral region. The reconstructions were performed on chemical images representing the intensity of the band at 1077 cm^{-1} and evaluated using a baseline spanning the region 980–1130 cm^{-1}.

ER-Tracker Stain—A separate set of live neurons from bilateral lumbar 1–6 ganglia (L1–6) DRGs from C57BL6/J and TRPA1 KO mice was stained with the endoplasmic reticulum

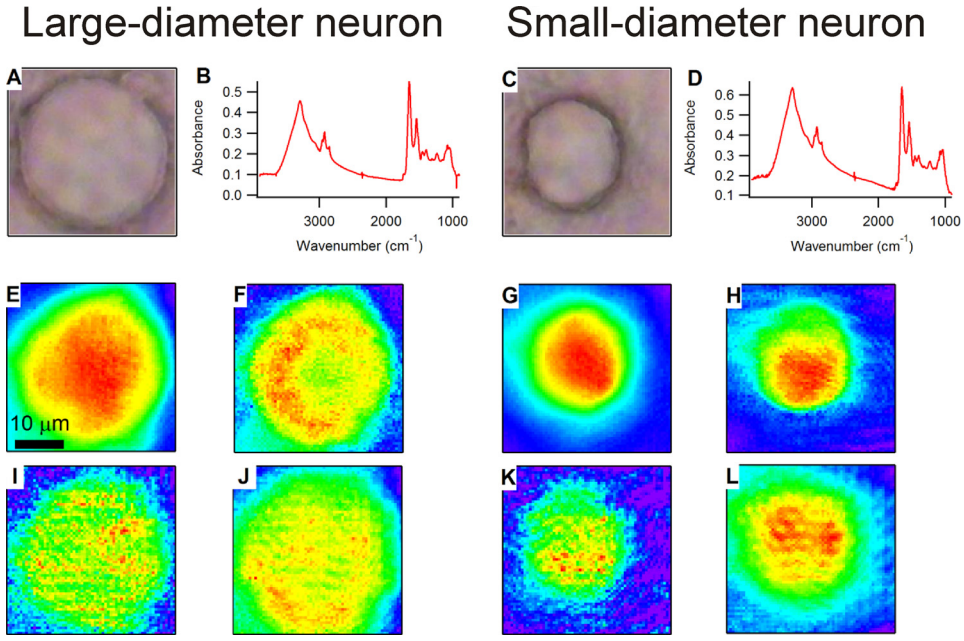

FIGURE 1. *A* and *C*, visible images of a representative large-diameter (*A*) and small-diameter (*C*) neuron. Average mid-infrared spectra of the respective neurons, generated by averaging the spectra from each pixel occupied by the somata, are shown in *B* and *D*. *E–L* show chemical images generated for amide (*E* and *G*), hydrocarbon (*F* and *H*), phosphate (*I* and *K*), and carbohydrate (*J* and *L*) for the large-diameter and small-diameter neurons, respectively. All of the visible and IR images represent a field of view that is the same size, so the *scale bar* in *E* represents 10 μm and applies to all images.

(ER)-Tracker (Invitrogen) according to the manufacturer's instructions. ER-Tracker (500 nM in Hanks' buffered saline solution) was applied for 15–20 min at 20 °C prior to imaging. A fluorescence signal considered positive was more intense than background fluorescence.

Statistics—The percentages of neurons with rings were analyzed using χ-square and Fisher's exact tests. Relative lipid content was analyzed using a one-way analysis of variance with Tukey's post hoc test. Error bars on graphs represent the S.E. p values <0.05 were considered significant.

RESULTS

This study was driven by three specific aims: 1) identify and characterize novel differences in chemistry of subpopulations of DRG sensory neurons, 2) determine whether peripheral inflammation induces changes in relative lipid content at the single-cell level, and 3) determine whether any changes during inflammation are dependent on an ion channel commonly associated with inflammatory pain, the TRPA1.

IR Spectra and Chemical Images of Representative Sensory and Non-sensory Neurons—To characterize the chemistry of native sensory neuron subpopulations, we compared spectra between small-diameter (<27 μm) and large-diameter (≥ 27 μm) somata from naive C57BL/6J (wild-type) mice (five independent primary culture preparations from six mice). Datasets consisting of 59 neurons were used to generate IR images. Here we present the spectra and chemical images of representative large-diameter and small-diameter neurons (Fig. 1). Fig. 1, *B* and *D*, compare spectra generated by averaging the spectra from each pixel occupied by the cell. The representative spectra of both neurons show the biological functional groups expected for a living cell, including amide, hydrocarbon, carbohydrate, phosphate, and water. The characteristic frequencies of these functional groups are discussed in detail elsewhere (46). In brief, we used the following spectral regions as indicators of specific functional groups: 2800–3000 cm^{-1} (C–H stretching of hydrocarbons, primarily lipids), 1600–1700 cm^{-1} (C=O stretching of amide functional groups in protein), 1200–1268 cm^{-1} (PO_2^- asymmetric stretching of phosphates in lipids, sugars, and nucleic acids), and 1000–1135 cm^{-1} (mixed C–O–H modes of carbohydrates). The region from 3000 to 3600 cm^{-1} has contributions from N–H stretching modes from proteins as well as O–H stretching modes from water and carbohydrates. Chemical images were generated by integrating the area under the spectral regions with a corresponding baseline at each pixel. The chemical images were pseudocolored to illustrate relative abundance or density of the corresponding functional groups such that *red* delineates regions of high relative abundance, and *blue* indicates areas of low relative abundance (Fig. 1, *E–L*).

In a portion of the sensory neurons (61%, 36/59), we observed distinctive ring-shaped structures in the chemical images. For example, the C–H chemical image of the representative large-diameter neuron (Fig. 1*F*) contains a region of relatively high intensity in a circular, ring-shaped distribution (seen in *red* and *yellow*) with a region of lower intensity at the very interior of the cell (in *green*). We refer to such a distribution as a "chemical ring." The chemical image of the carbohydrate distribution for the large-diameter neuron (Fig. 1*J*) shows a somewhat similar pattern, although the ring-shaped architecture is less clear. This apparent obscuration of the image is most likely due to the longer wavelength used to generate images from bands in the fingerprint region (a 9.5-μm wavelength used for chemical images of the C–OH stretching and C–O–H bending features of carbohydrates *versus* a 3-μm wavelength used for O–H stretching features). In contrast, in the chemical images for the

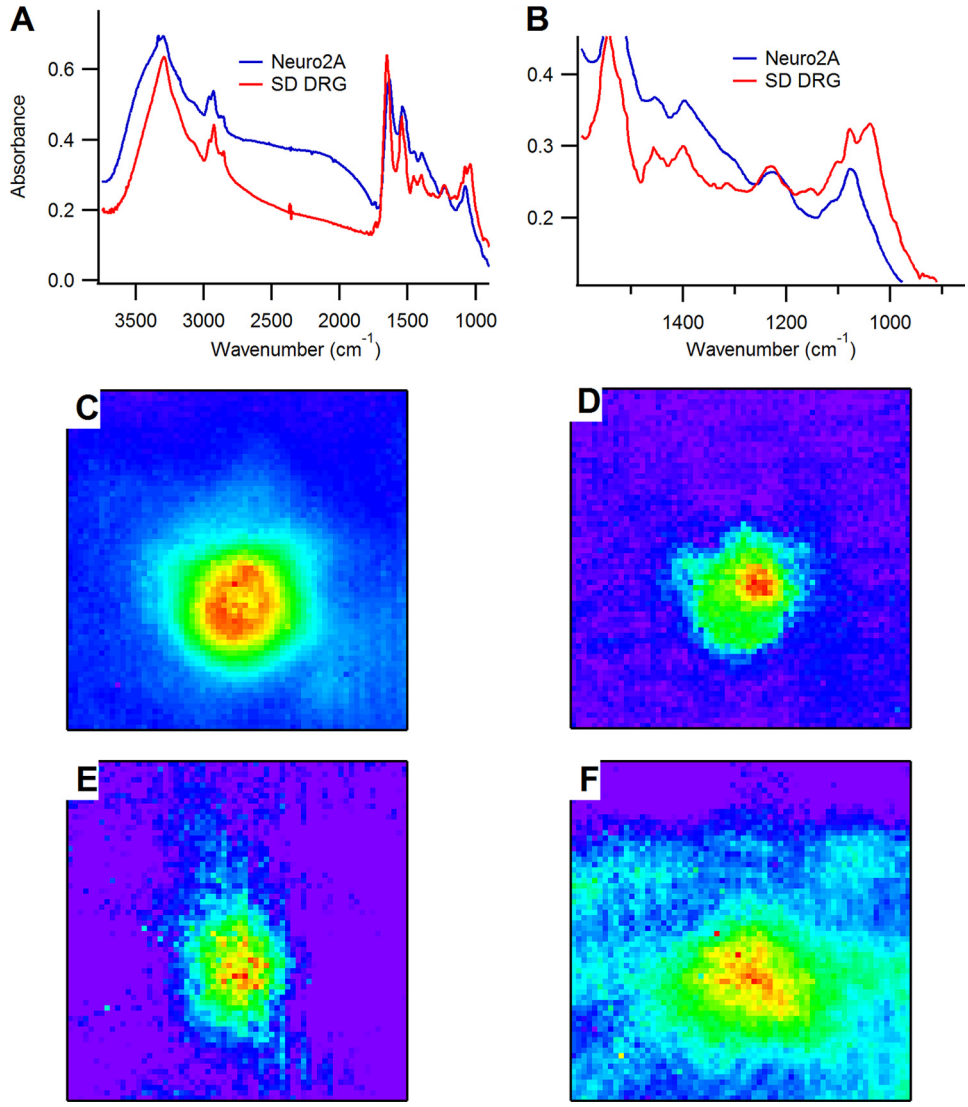

FIGURE 2. *A*, comparison of spectra from the small-diameter DRG (*SD DRG*) sensory neuron in Fig. 1 with that of a Neuro2A cell, with a close up of the fingerprint region shown in *B*. *C–F* show chemical images generated by integrating under absorption bands specific to lipid/C–H (*C*), amide (*D*), phosphate (*E*), and carbohydrate (*F*).

representative small-diameter neuron (Fig. 1, *G–L*), all of the chemical moieties imaged have a distribution that is (in projection) most intense in the center of the cell and gradually decreases to the thinner periphery of the cell. This representative small-diameter neuron would be considered to have no rings. These chemical ring features were unexpected and have not, to our knowledge, been characterized previously for any native cell type.

We performed analogous studies on non-sensory neurons (Neuro2A, ATCC CCL-131) to identify which characteristics are unique to DRG sensory neurons. Fig. 2 shows an analysis of a representative Neuro2A cell; in Fig. 2, *A* and *B*, we compare spectra (averaged over all the pixels comprising the cell body) of the Neuro2A cell from the spectrum of the small-diameter neuron in Fig. 1. The most pronounced differences are observed in the fingerprint region, where the small-diameter DRG neuron has a distinctive signature composed of several intense bands spanning the 1000–1150-cm^{-1} region due to carbohydrate moieties. In contrast, the Neuro2A cell has minimal contributions in this spectral region, with one sharp peak at 1080 cm^{-1} due to the phosphate symmetric stretching mode superimposed on a broad and very weak peak spanning the carbohydrate region. In light of the comparatively large carbohydrate signature observed in the DRG neurons relative to the Neuro2A cells, it is possible that the carbohydrate content observed in the DRGs may be specific to their sensory function. It is not possible to specify from the IR spectra exactly which chemical species of carbohydrates gives rise to the unique features in the 1000–1150-cm^{-1} region of the DRG spectra, but DRG neurons are known to express numerous glycoproteins such as those that contain α-D-galactose and bind isolectin B4. In Fig. 2, *C–F*, we show chemical images of the Neuro2A cell specific to C–H (2800–3000 cm^{-1}), amide (1600–1700 cm^{-1}), phosphate (1150–1265 cm^{-1}), and carbohydrate (1000–1100 cm^{-1}) functional groups. The images shown here are representative of the large pool of cells examined, which was largely homogeneous in the observed cell morphologies. In chemical images generated for all of the cells we observed, the apparent ring

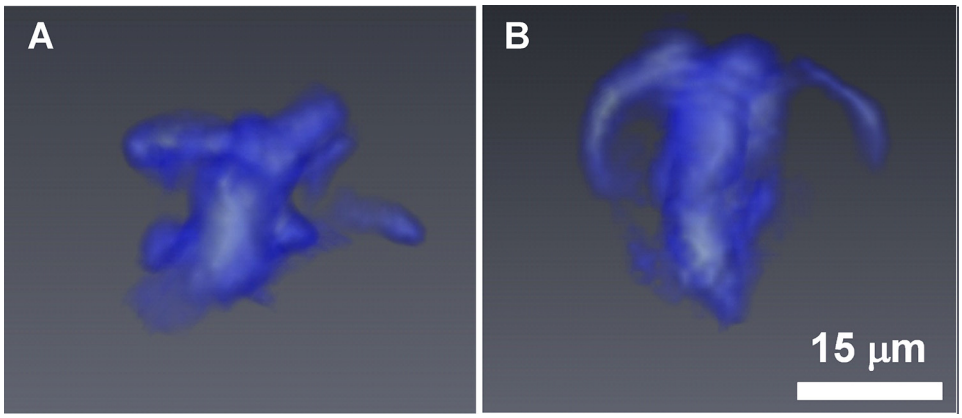

FIGURE 3. **Tomographic reconstructions of the three-dimensional carbohydrate distribution of a naive, WT DRG neuron ($n = 1$).** *A* and *B* represent perspective views of the cell from two orthogonal directions, where the side view (*A*) and top view (*B*) orientations are determined with respect to the plane of the microloop holder. The *white scale bar* in *B* represents 15 μm and also applies to *A*.

pattern was absent; rather, the cells present in the morphology more commonly observed in single cells where the greatest projected intensity is observed in the mid-body bulge and continuously decreases through the cytoplasm and to the membrane. Similar results can be observed in Refs. 47 and 48.

Correlated Infrared and Fluorescence Microscopy to Identify the Origin of Ring Distributions—In two-dimensional projection images, it is impossible to determine the three-dimensional distribution of the chemical rings. Therefore, we conducted IR spectro-microtomography to assess the three-dimensional structure of these chemical distributions in detail. Namely, we set out to determine whether the ring structures were intracellular or extracellular. We performed the spectro-microtomography experiments as described previously (40) on individual DRG neurons mounted onto polyimide microloop holders. Fig. 3 shows the three-dimensional tomographic reconstructions of chemical images generated from the carbohydrate spectral region as viewed from two orthogonal planes. We used the peak intensity at 1077 cm^{-1}, with 980–1130-cm^{-1} baseline. The 1000–1150-cm^{-1} region was chosen because this region of absorption spectra was clearly beyond the background absorption of the sample holder and is a spectral range in which we frequently observed chemical rings. Although only one dataset is presented, the three-dimensional distribution of the carbohydrates suggests that the ring structures in fact arise from intracellular architectures within the cytoplasm and form a tubular distribution, much like the morphology of the ER. Because the ER is known to be enriched with lipids and carbohydrates (49, 50), we hypothesized that the observed ring structures may arise from the subcellular structure of the ER.

To investigate whether the distribution of the ER correlates with the regions of the chemical rings, we stained live neurons with ER-Tracker Red (Molecular Probes) to fluorescently label the endoplasmic reticulum. Fig. 4 compares representative fluorescence images of the stained cells (Fig. 4, *A–C*) with an analogous set of cells observed in IR chemical images (Fig. 4*D*, showing C–H distribution). After reviewing many fluorescence images ($n = 20–30$ neurons) and comparing them with the integrated chemical images, we found overwhelming similarities between the morphology and structure of the ER as observed in the fluorescent images and the lipid and carbohydrate ring structures observed in the chemical images. As illustrated by the example here, and as corroborated in many other datasets, the stained ER and the annular lipid and carbohydrate structures appeared to be located in the same position within the cytoplasm of the neurons. These data strongly suggest that the ring structures observed in the chemical images are representative of the ER and indicate differential enrichment of lipid and/or carbohydrate in subpopulations of native somatosensory neurons.

Prevalence of Chemical Ring Subtypes Differs between Large- and Small-diameter Sensory Neurons—To assess the prevalence and subtypes of chemical rings in the sensory neuron subpopulations, we randomly imaged small-diameter ($n = 36$) and large-diameter ($n = 23$) neurons from five independent cell culture preparations from six naive wild-type mice. We generated chemical images of hydrocarbon, amide, phosphate, O–H/N–H, and carbohydrate to evaluate the prevalence of these subcellular ring structures, and the results are shown in Fig. 5 and summarized in Table 1. Annular or ringed chemical distributions were frequently observed in the images generated from O–H/N–H, C–H stretching, lipid C=O (1715–1770 cm^{-1}), phosphate (1200–1300 cm^{-1}), and carbohydrate (1000–1120 cm^{-1}), but never observed in the chemical images of the amide distribution. Thus, the ring structures are chemically specific in that they are attributable only to certain functional groups, such as lipids/CH and carbohydrates/OH but not amides. Therefore, the chemical rings are not imaging artifacts or due to differences in the shape of the cells (thickness or volume).

Assessment of chemical rings was conducted by experimenters blinded to treatment, genotype, and cell size. We found that images generated from both the carbohydrate C–O–H signatures and the O–H/N–H stretching signatures showed similar intensity distributions in most cases. We noted, however, that the C–OH stretching chemical images had significantly lower spatial resolution because the wavelength of the probe light is three times longer. The sometimes subtle features of the ring structure generally appeared sharper in the O–H stretching images, so we equated the rings observed in chemical images generated from O–H stretching modes with carbohydrate images for the purpose of quantifying the prevalence of rings. This is justified by the correlation we observed between O–H

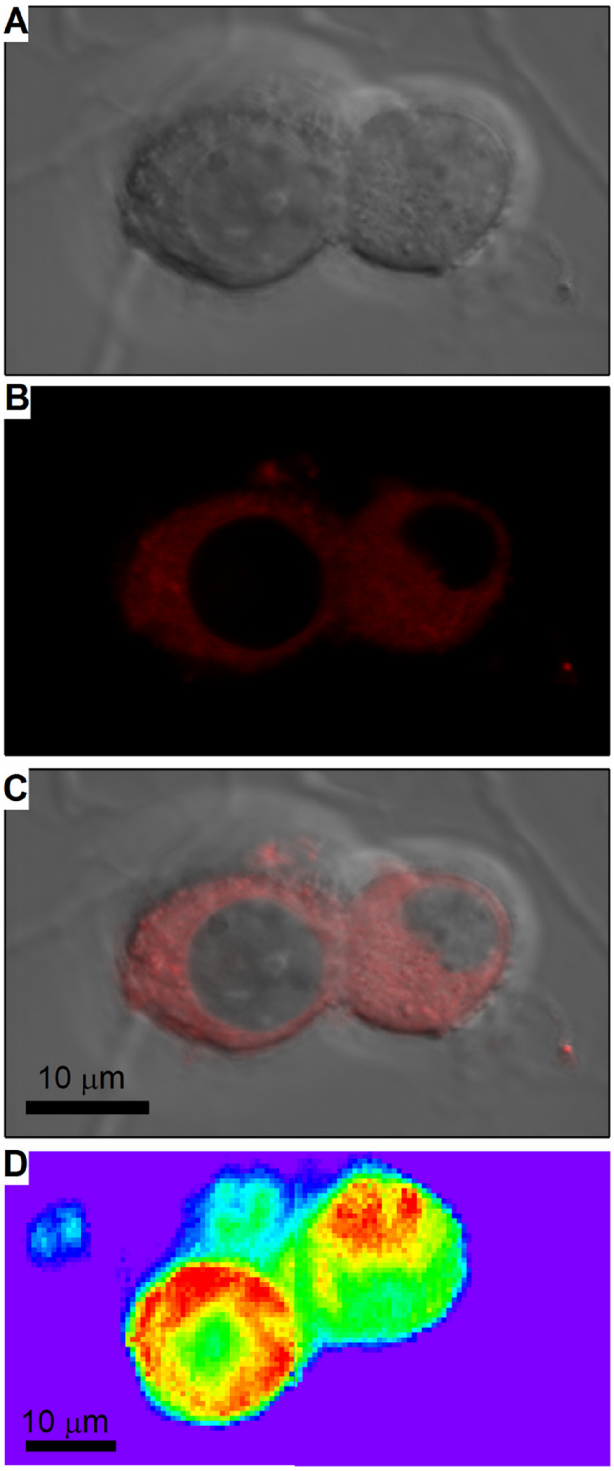

FIGURE 4. **Images of DRG neurons.** *A*, visible image of neurons. *B*, ER-Tracker-stained neurons. *C*, overlay of visible and fluorescent images. *D*, IR images of a pair of neurons that have analogous morphology, as seen from IR contrast, to those in the fluorescence images in *A–C*. The image is generated from integrating the C–H stretching region (2800–3000 cm^{-1} with corresponding baseline). The left cell in *D* corresponds to the left cell in *A–C*, where a ring that is almost uniform is observed around the nucleus. The right cell in *D* corresponds to the right cell in *A–C*, but with the position of the nucleus rotated 90° clockwise. The *black scale bars* in *C* and *D* represent 10 μm and apply to all images.

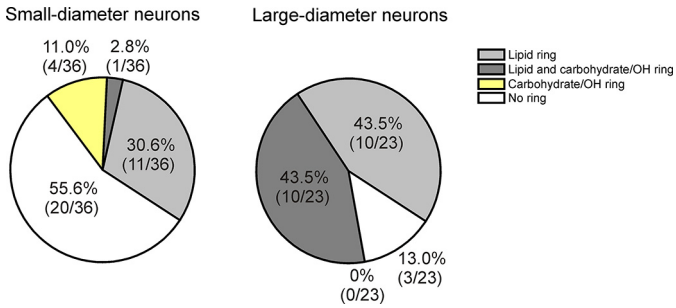

FIGURE 5. **Prevalence of chemical ring subtypes is significantly different between large-diameter and small-diameter DRG neurons (overall $p < 0.0001$ χ-square).** Significantly more large-diameter neurons (86.4%; 19/22) contain chemical rings than in small-diameter neurons (46.2%; 27/37; $p = 0.0024$, Fisher's exact tests). Nearly half of the large-diameter neurons (45.5%; 10/22) contain rings enriched in both lipids and carbohydrates (45.5%; 10/22), and few small-diameter neurons contain rings with lipids and carbohydrates (2.7%; 1/37; $p < 0.0001$, Fisher's exact tests).

TABLE 1

Assessment of chemical images to identify the prevalence of chemical "ring" structures in different subpopulations of DRG neurons

	No ring	Lipid ring	Carbohydrate ring	Carbohydrate and lipid ring
			%	
Small, WT, naive	72.2 (39/54)	1.85 (1/54)	22.2 (12/54)	3.7 (2/54)
Large, WT, naive	12.8 (5/39)	10.26 (4/39)	25.6 (10/39)	54.28 (20/39)
Small, WT, CFA	61.54 (24/39)	7.96 (3/39)	15.38 (6/39)	15.38 (6/39)
Large, WT, CFA	10.53 (2/19)	0 (0/19)	41.58 (6/19)	57.89 (11/19)
Small, TRPA1 KO, naive	68.43 (26/38)	2.63 (1/38)	23.68 (9/38)	5.26 (2/38)
Large, TRPA1 KO, Naïve	25 (8/32)	0 (0/32)	25 (8/32)	50 (16/32)
Small, TRPA1 KO, CFA	69.23 (27/39)	10.25 (4/39)	10.26 (4/39)	10.26 (4/39)
Large, TRPA1 KO, CFA	10 (2/20)	35 (7/20)	10 (2/20)	45 (9/20)

stretching and C–O–H stretching/bending chemical images in the datasets. Thus, we were able to conclude that the observation of the O–H ring was indicative of a carbohydrate ring and not another species, such as water or amide, that absorbs in the same spectral region. Neurons that exhibited a ring structure in the C–O–H region (1000–1150 cm^{-1}) or the O–H stretching region (3000–3600 cm^{-1}) were considered to have a carbohydrate ring.

We observed marked differences in the abundance of ring structures between small- and large-diameter neurons (Fig. 5; overall χ-square $p < 0.0001$). Significantly more large-diameter neurons (87; 20/23) contain chemical rings than small-diameter neurons (44.4%; 16/36; $p = 0.0012$, Fisher's exact tests). There was no difference in cell size between small-diameter neurons that exhibit a chemical ring and those without rings. Similarly, large-diameter neurons with and without rings were also the same size. Therefore, the finding that chemical rings were more prevalent in large-diameter neurons than small-diameter neurons was likely not due to cell size affecting our ability to resolve a ring structure.

We then compared the prevalence of subtypes of chemical rings between small- and large-diameter neurons. Similar percentages of large- and small-diameter neurons contain carbohydrate/OH-enriched chemical rings (Fig. 5, *light gray*). None of the large-diameter neurons (0/23) and few small-diameter neurons (4/36) contain a ring consisting only of lipid enrichment (*yellow*, not significant). Interestingly, large-diameter neurons frequently contain rings enriched in both lipids and carbohydrates (43.5%; 10/23), whereas small-diameter neurons rarely contain this subtype of ring (2.8%; 1/36; $p < 0.0002$, Fisher's exact tests; *dark gray*). We performed similar analyses of neurons from wild-type mice with CFA inflammation ($n = 7$ mice; 63 total neurons), TRPA1 KO mice ($n = 5$; 69), and

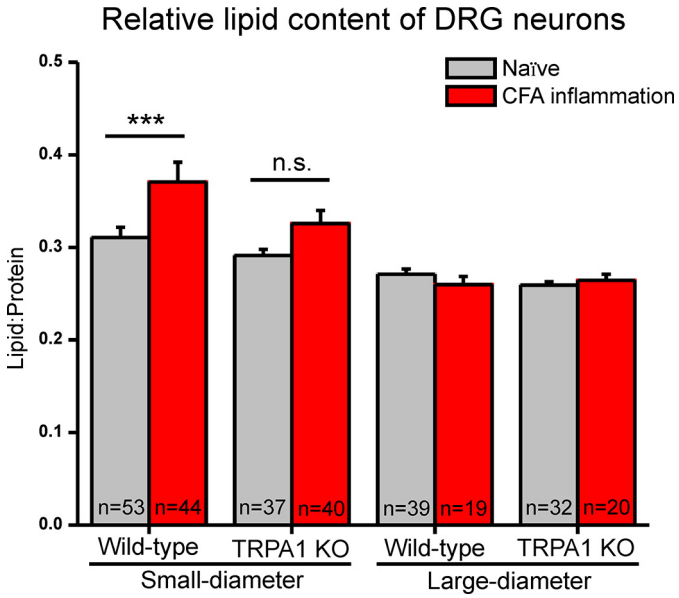

FIGURE 6. **Relative lipid content for small- and large-diameter neurons from naive and CFA inflamed wild-type and TRPA1 KO mice.** Relative lipid content significantly increases with CFA inflammation in small-diameter wild-type neurons (overall $p < 0.0001$ one-way analysis of variance; ***, $p < 0.001$ Tukey's post hoc test), whereas small-diameter TRPA1 KO neurons did not exhibit an increase with inflammation (not significant (*n.s.*); $p > 0.05$). There were no significant differences in large-diameter neurons of wild-type and TRPA1 KO mice. *Error bars* represent S.E.

TRPA1 KO mice with CFA ($n = 8$; 60), but found no significant differences due to treatment or genotype. This indicates that neither the TRPA1 channel nor inflammation modulates the presence of the chemical rings.

Relative Lipid Content Increase in Small-diameter Neurons during Inflammation Is Dependent on TRPA1—We calculated the relative lipid content, defined as the ratio of the integrated area of the C–H absorption bands to that of the amide I absorption band, for each neuron. The following process was used to perform these calculations. First, we extracted the spectra from each pixel occupied by the cell. These spectra were then averaged to obtain a single average IR spectrum for each cell. Next, integrated areas of the C–H (2800–3000 cm^{-1}) and amide I (1600–1700 cm^{-1}) bands, with a linear baseline used at the endpoints, were calculated from these average spectra. The ratio of the CH:amide I areas was used to establish the relative lipid content for each cell. IR absorption follows a Beer's law-type behavior, meaning that the measured absorbance is directly proportional to the concentration of the analyte being considered. Although the relative lipid content is not an absolute measurement of the lipid concentration within the cell, the *change* in the relative lipid content is directly proportional to the change in concentration of the CH_x functional groups relative to the cellular protein content within the cells among the different subpopulations considered.

In Fig. 6, we present the relative lipid content for several subpopulations of DRG neurons, segregated by size (large- and small-diameter), treatment (naive and CFA inflammation), and genotype (wild type and TRPA1 KO). At least three independent preparations were conducted per group consisting of DRGs from a total of six wild-type naive, seven wild-type CFA, five TRPA1 KO naive, and eight TRPA1 CFA mice. Small-diameter wild-type neurons showed a significant increase in the relative lipid content following inflammation (a 20% increase in the concentration of CH_x functional groups within the cell; overall $p < 0.0001$ one-way analysis of variance; ***, $p < 0.001$ Tukey's post hoc test). There was no significant difference in the relative lipid content of large-diameter neurons of any genotype or treatment (wild type, TRPA1 KO, naive, or CFA). Also, there was no significant difference in the relative lipid content of neurons with lipid- and/or carbohydrate-enriched rings and those without rings.

The TRPA1 protein channel is expressed by a subpopulation of small-diameter DRG neurons and mediates sensitization to mechanical and cold stimuli during CFA inflammation (33, 37, 51–54). Because TRPA1 plays a major role in inflammatory pain, we wanted to determine whether the increase in relative lipid content observed in small-diameter neuron during inflammation might be dependent on TRPA1. Therefore, we compared the results from wild-type neurons with neurons from naive and CFA-injected TRPA1 KO mice. In small-diameter, wild-type neurons, we observed a significant ($p < 0.001$) increase in relative lipid content following CFA inflammation as compared with naive control neurons (Fig. 6). Interestingly, this effect was diminished in TRPA1 KO neurons, where following inflammation, the change in the relative lipid content failed to reach statistical significance ($p = 0.062$). This difference in the effect of inflammation on TRPA1 KO *versus* wild-type neurons suggests that the increase in lipid content during inflammation is dependent in part on the expression TRPA1.

DISCUSSION

The potential role of lipids and carbohydrates in sensory transduction is understudied. However, lipids and carbohydrates have been shown to influence the excitability of DRG neurons (20–26). Recently, altered lipid metabolism pathways have been implicated in nerve injury-induced and inflammatory pain (27–29). Lipid or lipid-protein interactions may affect the mechanotransduction ion channel properties of sensory neurons as these properties are typically studied by focal probing of the plasma membrane (55–57). Lipids may also function in inflammatory pain. Therefore, it is important to consider the influence of lipids and carbohydrates in sensory neuron function in naive animals and during inflammation.

This study identified novel annular distributions of lipid and/or carbohydrate enrichment in sensory neurons. Due to the similar distributions of fluorescent labeling and chemical rings and the function of the ER in lipid and carbohydrate metabolism, we attribute the observed lipid, carbohydrate, and phosphate rings to the ER. We found that chemical morphology can define subpopulations of sensory neurons based on lipid and/or carbohydrate enrichment in chemical rings. This is the first report of differential enrichment of the ER within subpopulations of DRG neurons. We also note that the failure of the Neuro2A cells to reproduce the observed differential ER enrichment suggests that this property is unique to sensory neurons. The differences in the prevalence of chemical ring subtypes between small- and large-diameter neurons might correlate with the functional differences between these two neuronal types. Whether these subpopulations of neurons are

functionally distinct or whether the chemical rings have any impact on functional properties remains to be elucidated.

Sensitization of subpopulations of DRG sensory neurons during peripheral inflammation contributes substantially to inflammatory pain (33, 52–54, 58, 59). Therefore, we hypothesized that the changes in chemical composition during inflammation might relate to the functional changes, such as the sensitization of sensory neurons that occur during inflammation. We found that inflammation induces significant increases in relative lipid content specifically in wild-type, small-diameter neurons. TRPA1 is predominantly expressed by small-diameter neurons (35, 51, 60), and TRPA1 sensitization within this subpopulation of sensory neurons underlies mechanical and cold hypersensitivity during inflammation (33, 37, 51–54, 58, 59). We note, however, a small, statistically insignificant, increase in relative lipid content in TRPA1 KO small-diameter neurons, suggesting the possibility that protein(s) other than TRPA1 may contribute to this effect.

We considered the possibility that the increased relative lipid content in small-diameter wild-type neurons is due to differences between the anatomical levels of the DRG (lumbar 1–6 for naive *versus* lumbar 3–5 for CFA). Therefore, we performed additional control measurements (not shown) using an in-house IR source to compare lumbar 1–6 ganglia and lumbar 3–5 ganglia (L3–5) DRGs and found no significant difference in relative lipid content between these groups.

Although it is unlikely, it is possible that the incorporation of the CFA oil resulted in specific changes to wild-type small-diameter neurons and not in TRPA1 KO neurons. We did not determine whether the increase in lipids occurs throughout the neuron and its processes or solely in the soma. However, isolated sensory neuron somata are a common and widely used model for functional assays such as calcium imaging and patch clamp electrophysiology (35–39). Therefore, it is important to identify, define, and understand changes that occur in DRG somata in this *in vitro* setting.

Several lipid mediators are known to sensitize the TRPA1 channel (61–64). However, our findings are the first to indicate that TRPA1 may mediate lipid biosynthesis and/or incorporation in sensory neurons during inflammation. Altered lipid metabolism has been implicated in chronic neuropathic and inflammatory pain (27–29). This is the first study to indicate that this may also be true for inflammatory pain. Therefore, these findings may have important implications linking lipids and inflammatory pain.

Acknowledgments—We acknowledge Amanda Smith and Crystal O'Hara for technical assistance in cell culture. IRENI was partially supported by the Forest Service and Forest Products Laboratory. IRENI was developed under NSF Grant MRI-DMR-0619759. The SRC was funded by University of Wisconsin-Milwaukee and University of Wisconsin-Madison.

REFERENCES

1. Basbaum, A. I., Bautista, D. M., Scherrer, G., and Julius, D. (2009) Cellular and molecular mechanisms of pain. *Cell* **139,** 267–284
2. Lumpkin, E. A., and Caterina, M. J. (2007) Mechanisms of sensory transduction in the skin. *Nature* **445,** 858–865
3. Gascon, E., and Moqrich, A. (2010) Heterogeneity in primary nociceptive neurons: from molecules to pathology. *Arch. Pharm. Res.* **33,** 1489–1507
4. Le Pichon, C. E., and Chesler, A. T. (2014) The functional and anatomical dissection of somatosensory subpopulations using mouse genetics. *Front. Neuroanat.* **8,** 21
5. Abraira, V. E., and Ginty, D. D. (2013) The sensory neurons of touch. *Neuron* **79,** 618–639
6. Zylka, M. J., Rice, F. L., and Anderson, D. J. (2005) Topographically distinct epidermal nociceptive circuits revealed by axonal tracers targeted to *Mrgprd*. *Neuron* **45,** 17–25
7. Dubin, A. E., and Patapoutian, A. (2010) Nociceptors: the sensors of the pain pathway. *J. Clin. Invest.* **120,** 3760–3772
8. Hjerling-Leffler, J., Alqatari, M., Ernfors, P., and Koltzenburg, M. (2007) Emergence of functional sensory subtypes as defined by transient receptor potential channel expression. *J. Neurosci.* **27,** 2435–2443
9. Caterina, M. J., Schumacher, M. A., Tominaga, M., Rosen, T. A., Levine, J. D., and Julius, D. (1997) The capsaicin receptor: a heat-activated ion channel in the pain pathway. *Nature* **389,** 816–824
10. Gavva, N. R., Bannon, A. W., Surapaneni, S., Hovland, D. N., Jr., Lehto, S. G., Gore, A., Juan, T., Deng, H., Han, B., Klionsky, L., Kuang, R., Le, A., Tamir, R., Wang, J., Youngblood, B., Zhu, D., Norman, M. H., Magal, E., Treanor, J. J. S., and Louis, J. C. (2007) The vanilloid receptor TRPV1 is tonically activated *in vivo* and involved in body temperature regulation. *J. Neurosci.* **27,** 3366–3374
11. Stucky, C. L., Dubin, A. E., Jeske, N. A., Malin, S. A., McKemy, D. D., and Story, G. M. (2009) Roles of transient receptor potential channels in pain. *Brain Res. Rev.* **60,** 2–23
12. Ritter, A. M., and Mendell, L. M. (1992) Somal membrane properties of physiologically identified sensory neurons in the rat effects of nerve growth factor. *J. Neurophysiol.* **68,** 2033–2041
13. Lawson, S. N., and Waddell, P. J. (1991) Soma neurofilament immunoreactivity is related to cell size and fibre conduction velocity in rat primary sensory neurons. *J. Physiol.* **435,** 41–63
14. Lawson, S. N., Perry, M. J., Prabhakar, E., and McCarthy, P. W. (1993) Primary sensory neurons, neurofilament, neuropeptides and conduction velocity. *Brain Res. Bull.* **30,** 239–243
15. Reichling, D. B., and Levine, J. D. (2009) Critical role of nociceptor plasticity in chronic pain. *Trends Neurosci.* **32,** 611–618
16. Ferraro, J. T., Daneshmand, M., Bizios, R., and Rizzo, V. (2004) Depletion of plasma membrane cholesterol dampens hydrostatic pressure and shear stress-induced mechanotransduction pathways in osteoblast cultures. *Am. J. Physiol. Cell Physiol.* **286,** C831–C839
17. Xing, Y., Gu, Y., Xu, L. C., Siedlecki, C. A., Donahue, H. J., and You, J. (2011) Effects of membrane cholesterol depletion and GPI-anchored protein reduction on osteoblastic mechanotransduction. *J. Cell Physiol.* **226,** 2350–2359
18. Wang, Y., Maciejewski, B. S., Drouillard, D., Santos, M., Hokenson, M. A., Hawwa, R. L., Huang, Z., and Sanchez-Esteban, J. (2010) A role for caveolin-1 in mechanotransduction of fetal type II epithelial cells. *Am. J. Physiol. Lung Cell. Mol. Physiol.* **298,** L775–L783
19. Pahakis, M. Y., Kosky, J. R., Dull, R. O., and Tarbell, J. M. (2007) The role of endothelial glycocalyx components in mechanotransduction of fluid shear stress. *Biochem. Biophys. Res. Commun.* **355,** 228–233
20. Gnanasekaran, A., Sundukova, M., van den Maagdenberg, A. M. J. M., Fabbretti, E., and Nistri, A. (2011) Lipid rafts control P2X3 receptor distribution and function in trigeminal sensory neurons of a transgenic migraine mouse model. *Mol. Pain* **7,** 77
21. Szoke, E., Börzsei, R., Tóth, D. M., Lengl, O., Helyes, Z., Sándor, Z., and Szolcsányi, J. (2010) Effect of lipid raft disruption on TRPV1 receptor activation of trigeminal sensory neurons and transfected cell line. *Eur. J. Pharmacol.* **628,** 67–74
22. Pristerà, A., Baker, M. D., and Okuse, K. (2012) Association between tetrodotoxin resistant channels and lipid rafts regulates sensory neuron excitability. *PLoS One* **7,** e40079
23. Zhang, Y. H., Khanna, R., and Nicol, G. D. (2013) Nerve growth factor/p75 neurotrophin receptor-mediated sensitization of rat sensory neurons depends on membrane cholesterol. *Neuroscience* **248,** 562–570
24. Peng, X. Q., Zhang, X. L., Fang, Y., Xie, W. R., and Xie, Y. K. (2004) Sialic acid contributes to hyperexcitability of dorsal root ganglion neurons in

rats with peripheral nerve injury. *Brain Res.* **1026,** 185–193
25. Tyrrell, L., Renganathan, M., Dib-Hajj, S. D., and Waxman, S. G. (2001) Glycosylation alters steady-state inactivation of sodium channel $Na_v1.9$/NaN in dorsal root ganglion neurons and is developmentally regulated. *J. Neurosci.* **21,** 9629–9637
26. Li, C. X., Jing, Y. L., and Xie, Y. K. (2007) Glycosylation-induced depolarization facilitates subthreshold membrane oscillation in injured primary sensory neurons. *Brain Res.* **1139,** 201–209
27. Patti, G. J., Yanes, O., Shriver, L. P., Courade, J. P., Tautenhahn, R., Manchester, M., and Siuzdak, G. (2012) Metabolomics implicates altered sphingolipids in chronic pain of neuropathic origin. *Nat. Chem. Biol.* **8,** 232–234
28. Xu, Z.-Z., Berta, T., and Ji, R.-R. (2013) Resolvin E1 inhibits neuropathic pain and spinal cord microglial activation following peripheral nerve injury. *J. Neuroimmune Pharmacol.* **8,** 37–41
29. Piomelli, D., and Sasso, O. (2014) Peripheral gating of pain signals by endogenous lipid mediators. *Nat. Neurosci.* **17,** 164–174
30. Nasse, M. J., Walsh, M. J., Mattson, E. C., Reininger, R., Kajdacsy-Balla, A., Macias, V., Bhargava, R., and Hirschmugl, C. J. (2011) High-resolution Fourier-transform infrared chemical imaging with multiple synchrotron beams. *Nat. Methods* **8,** 413–416
31. Kastyak-Ibrahim, M. Z., Nasse, M. J., Rak, M., Hirschmugl, C., Del Bigio, M. R., Albensi, B. C., and Gough, K. M. (2012) Biochemical label-free tissue imaging with subcellular-resolution synchrotron FTIR with focal plane array detector. *Neuroimage* **60,** 376–383
32. Kwan, K. Y., Allchorne, A. J., Vollrath, M. A., Christensen, A. P., Zhang, D. S., Woolf, C. J., and Corey, D. P. (2006) TRPA1 contributes to cold, mechanical, and chemical nociception but is not essential for hair-cell transduction. *Neuron* **50,** 277–289
33. Lennertz, R. C., Kossyreva, E. A., Smith, A. K., and Stucky, C. L. (2012) TRPA1 mediates mechanical sensitization in nociceptors during inflammation. *PLoS One* **7,** e43597
34. Barabas, M. E., and Stucky, C. L. (2013) TRPV1, but not TRPA1, in primary sensory neurons contributes to cutaneous incision-mediated hypersensitivity. *Mol. Pain* **9,** 9
35. Barabas, M. E., Kossyreva, E. A., and Stucky, C. L. (2012) TRPA1 is functionally expressed primarily by IB4-binding, non-peptidergic mouse and rat sensory neurons. *PLoS One* **7,** e47988
36. Gold, M. S., Reichling, D. B., Shuster, M. J., and Levine, J. D. (1996) Hyperalgesic agents increase a tetrodotoxin-resistant Na^+ current in nociceptors. *Proc. Natl. Acad. Sci. U.S.A.* **93,** 1108–1112
37. Bautista, D. M., Jordt, S. E., Nikai, T., Tsuruda, P. R., Read, A. J., Poblete, J., Yamoah, E. N., Basbaum, A. I., and Julius, D. (2006) TRPA1 mediates the inflammatory actions of environmental irritants and proalgesic agents. *Cell* **124,** 1269–1282
38. Zurborg, S., Yurgionas, B., Jira, J. A., Caspani, O., and Heppenstall, P. A. (2007) Direct activation of the ion channel TRPA1 by Ca^{2+}. *Nat. Neurosci.* **10,** 277–279
39. Vilceanu, D., and Stucky, C. L. (2010) TRPA1 mediates mechanical currents in the plasma membrane of mouse sensory neurons. *PLoS One* **5,** e12177
40. Martin, M. C., Dabat-Blondeau, C., Unger, M., Sedlmair, J., Parkinson, D. Y., Bechtel, H. A., Illman, B., Castro, J. M., Keiluweit, M., Buschke, D., Ogle, B., Nasse, M. J., and Hirschmugl, C. J. (2013) 3D spectral imaging with synchrotron Fourier transform infrared spectro-microtomography. *Nat. Methods* **10,** 861–864
41. Erdoăn, H., and Fessler, J. A. (1999) Monotonic algorithms for transmission tomography. *IEEE Trans. Med. Imaging* **18,** 801–814
42. Erdogan, H., and Fessler, J. A. (1999) Ordered subsets algorithms for transmission tomography. *Phys. Med. Biol.* **44,** 2835–2851
43. Fessler, J. A., Ficaro, E. P., Clinthorne, N. H., and Lange, K. (1997) Grouped-coordinate ascent algorithms for penalized-likelihood transmission image reconstruction. *IEEE Trans. Med. Imaging* **16,** 166–175
44. Fessler, J. A., and Rogers, W. L. (1996) Spatial resolution properties of penalized-likelihood image reconstruction: space-invariant tomographs. *IEEE Trans Image Process.* **5,** 1346–1358
45. Stayman, J. W., and Fessler, J. A. (2000) Regularization for uniform spatial resolution properties in penalized-likelihood image reconstruction. *IEEE Trans. Med. Imaging* **19,** 601–615
46. Stuart, B. H. (2004) *Infrared Spectroscopy: Fundamentals and Applications*, John Wiley & Sons, Chichester, UK
47. Hackett, M. J., Borondics, F., Brown, D., Hirschmugl, C., Smith, S. E., Paterson, P. G., Nichol, H., Pickering, I. J., and George, G. N. (2013) Subcellular biochemical investigation of purkinje neurons using synchrotron radiation Fourier transform infrared spectroscopic imaging with a focal plane array detector. *ACS Chem. Neurosci.* **4,** 1071–1080
48. Sandt, C., Frederick, J., and Dumas, P. (2013) Profiling pluripotent stem cells and organelles using synchrotron radiation infrared microspectroscopy. *J. Biophotonics* **6,** 60–72
49. Hebert, D. N., Garman, S. C., and Molinari, M. (2005) The glycan code of the endoplasmic reticulum: asparagine-linked carbohydrates as protein maturation and quality-control tags. *Trends Cell Biol.* **15,** 364–370
50. Fagone, P., and Jackowski, S. (2009) Membrane phospholipid synthesis and endoplasmic reticulum function. *J. Lipid Res.* **50,** S311–S316
51. Story, G. M., Peier, A. M., Reeve, A. J., Eid, S. R., Mosbacher, J., Hricik, T. R., Earley, T. J., Hergarden, A. C., Andersson, D. A., Hwang, S. W., McIntyre, P., Jegla, T., Bevan, S., and Patapoutian, A. (2003) ANKTM1, a TRP-like channel expressed in nociceptive neurons, is activated by cold temperatures. *Cell* **112,** 819–829
52. Obata, K., Katsura, H., Mizushima, T., Yamanaka, H., Kobayashi, K., Dai, Y., Fukuoka, T., Tokunaga, A., Tominaga, M., and Noguchi, K. (2005) TRPA1 induced in sensory neurons contributes to cold hyperalgesia after inflammation and nerve injury. *J. Clin. Invest.* **115,** 2393–2401
53. Petrus, M., Peier, A. M., Bandell, M., Hwang, S. W., Huynh, T., Olney, N., Jegla, T., and Patapoutian, A. (2007) A role of TRPA1 in mechanical hyperalgesia is revealed by pharmacological inhibition. *Mol. Pain* **3,** 40
54. da Costa, D. S. M., Meotti, F. C., Andrade, E. L., Leal, P. C., Motta, E. M., and Calixto, J. B. (2010) The involvement of the transient receptor potential A1 (TRPA1) in the maintenance of mechanical and cold hyperalgesia in persistent inflammation. *Pain* **148,** 431–437
55. Vásquez, V., Krieg, M., Lockhead, D., and Goodman, M. B. (2014) Phospholipids that contain polyunsaturated fatty acids enhance neuronal cell mechanics and touch sensation. *Cell Rep.* **6,** 70–80
56. Anishkin, A., Loukin S. H., Teng J., and Kung C. (2014) Feeling the hidden mechanical forces in lipid bilayer is an original sense. *Proc. Natl. Acad. Sci. U.S.A.* **111,** 7898–7905
57. Poole, K., Moroni, M., and Lewin G. R. (2014) Sensory mechanotransduction at the membrane-matrix interfaces. *Pflugers Arch-Eur. J. Physiol.* 10.1007/s00424-014-1563-6
58. Breese, N. M., George, A. C., Pauers, L. E., and Stucky, C. L. (2005) Peripheral inflammation selectively increases TRPV1 function in IB4-positive sensory neurons from adult mouse. *Pain* **115,** 37–49
59. Dai, Y., Wang, S., Tominaga, M., Yamamoto, S., Fukuoka, T., Higashi, T., Kobayashi, K., Obata, K., Yamanaka, H., and Noguchi, K. (2007) Sensitization of TRPA1 by PAR2 contributes to the sensation of inflammatory pain. *J. Clin. Invest.* **117,** 1979–1987
60. Bandell, M., Story, G. M., Hwang, S. W., Viswanath, V., Eid, S. R., Petrus, M. J., Earley, T. J., and Patapoutian, A. (2004) Noxious cold ion channel TRPA1 is activated by pungent compounds and bradykinin. *Neuron* **41,** 849–857
61. Dall'Acqua, M. C., Bonet, I. J. M., Zampronio, A. R., Tambeli, C. H., Parada, C. A., and Fischer, L. (2014) The contribution of transient receptor potential ankyrin 1 (TRPA1) to the *in vivo* nociceptive effects of prostaglandin E-2. *Life Sci.* **105,** 7–13
62. Cruz-Orengo, L., Dhaka, A., Heuermann, R. J., Young, T. J., Montana, M. C., Cavanaugh, E. J., Kim, D., and Story, G. M. (2008) Cutaneous nociception evoked by 15-delta PGJ2 via activation of ion channel TRPAI. *Mol. Pain* **4,** 30
63. Materazzi, S., Nassini, R., Andrè, E., Campi, B., Amadesi, S., Trevisani, M., Bunnett, N. W., Patacchini, R., and Geppetti, P. (2008) Cox-dependent fatty acid metabolites cause pain through activation of the irritant receptor TRPA1. *Proc. Natl. Acad. Sci. U.S.A.* **105,** 12045–12050
64. Taylor-Clark, T. E., Undem, B. J., Macglashan, D. W., Jr., Ghatta, S., Carr, M. J., and McAlexander, M. A. (2008) Prostaglandin-induced activation of nociceptive neurons via direct interaction with transient receptor potential A1 (TRPA1). *Mol. Pharmacol.* **73,** 274–281